



HAL
open science

Dynamics of droplet coalescence on a vibrating vertical surface

Xiangshu Lei, Yingwen Liu, Peng Yang, Laurent Royon, Xiaofeng Guo

► **To cite this version:**

Xiangshu Lei, Yingwen Liu, Peng Yang, Laurent Royon, Xiaofeng Guo. Dynamics of droplet coalescence on a vibrating vertical surface. *Physics of Fluids*, 2023, 35 (7), pp.072102. 10.1063/5.0157591 . hal-04156027

HAL Id: hal-04156027

<https://hal.science/hal-04156027v1>

Submitted on 7 Jul 2023

HAL is a multi-disciplinary open access archive for the deposit and dissemination of scientific research documents, whether they are published or not. The documents may come from teaching and research institutions in France or abroad, or from public or private research centers.

L'archive ouverte pluridisciplinaire **HAL**, est destinée au dépôt et à la diffusion de documents scientifiques de niveau recherche, publiés ou non, émanant des établissements d'enseignement et de recherche français ou étrangers, des laboratoires publics ou privés.

This is the author's peer reviewed, accepted manuscript. However, the online version of record will be different from this version once it has been copyedited and typeset.

PLEASE CITE THIS ARTICLE AS DOI: 10.1063/5.0157591

Accepted to *Phys. Fluids* 10.1063/5.0157591

29 Vapor condensation is critical and common in urban environmental control,¹ power
30 generation,² food processing,³ as well as water recovery⁴⁻⁶ and treatment.⁷ Rising
31 energy costs, environmental impact and carbon emissions have aroused persistent
32 concerns over energy conservation in condensation processes. Considering the
33 important role that vapor condensing plays in industrial processes, a higher-
34 performance design of vapor condensation would be positive from both an economic
35 and environmental perspective.

36 Dropwise condensation (DWC) and filmwise condensation (FWC) are two common
37 modes of vapor condensation. In DWC, discrete droplets nucleate, grow, and then
38 coalesce on a cool surface. The extra surface that is not covered by droplets continues
39 to achieve condensation. In FWC, the whole surface is covered by a continuous
40 condensate film, which causes a rapid increase in thermal resistance. They could suffer
41 from ten-fold lower heat transfer coefficients (HTC) than in DWC.⁸ Moreover, reducing
42 the area of the drop-covered surface, as soon as nucleation begins, is the key to
43 achieving higher overall condensation HTC. For DWC on a vertical surface, when the
44 diameter of a droplet exceeds the capillary length, it can slide off by gravity. This
45 entrains other droplets during the sliding and refreshes extra condensation surface
46 exposed directly to vapor. Consequently, the key to enhancing DWC is to accelerate
47 drop removal, which is harder on randomly oriented surfaces.⁹

48 Superhydrophobic surfaces have been developed to promote sliding, detachment and
49 combination of small droplets.^{10, 11} When two neighboring drops coalesce, a
50 spontaneous jumping effect due to surface energy release is stimulated.¹² This is
51 reported to enhance condensation by an order of magnitude in HTC as compared to
52 DWC on an ordinary surface.¹³ Various micro/nanostructured superhydrophobic
53 surfaces can be obtained by chemical (etching, oxidation) or mechanical techniques
54 (additive manufacturing).¹⁴ However, the durability of these surfaces remains an issue,
55 as the structures and coatings tend to degrade rapidly under high temperature and
56 humidity conditions as well as scale deposits. Moreover, from the point of view of
57 condensate nucleation, hydrophobic surfaces require a higher degree of supersaturation
58 than ordinary surfaces.¹⁵ Increase in the overall performance is thus compromised, as a

This is the author's peer reviewed, accepted manuscript. However, the online version of record will be different from this version once it has been copyedited and typeset.

PLEASE CITE THIS ARTICLE AS DOI: 10.1063/5.0157591

Accepted to *Phys. Fluids* 10.1063/5.0157591

59 lower condensation source temperature is required. Therefore, active removal of
 60 droplets from ordinary surfaces is highly desirable.

61 Vibration of the condensation surface is an effective active technique which could
 62 overcome the above challenges. Droplet deformation and displacement driven by
 63 vibration are key mechanisms for promoting surface detachment. Depending on the
 64 direction, frequency and amplitude of vibration, droplets behave differently. On a
 65 horizontal surface vibrating along its normal direction, a backward motion of droplet is
 66 observed when vibration frequency is smaller than a quarter of the eigen frequency or
 67 within a narrow domain around 1.5 times eigen frequency.¹⁶ On a vertical surface
 68 vibrating along its longitudinal axis, if the vibration frequency is equal to the resonance
 69 frequency of the droplet, a maximal deformation can be obtained. In addition, if the
 70 amplitude of vibration is high, the deformation can overcome the contact angle
 71 hysteresis and the contact line starts to move.^{17, 18} The higher the contact angle, the
 72 greater this effect. Vibration in the transversal direction of the condensation surface also
 73 enhances detachment from superhydrophobic surfaces. As shown in Fig. 1(b) and (c),
 74 vertically and horizontally oriented substrates with superhydrophobic treatment are
 75 investigated respectively by Moradi et al.¹⁹ and Sun et al.²⁰ They achieved droplet
 76 detachment by high-amplitude vibration at the resonance frequency. Statistical results
 77 show a reduction in the average size of the departing droplet and a significant increase
 78 (by 8.6) in droplet sliding speed compared to non-vibrated ones.²¹ Consequences on the
 79 condensation heat transfer enhancement are noteworthy: heat transfer rate improves by
 80 more than 70% over the stationary case when longitudinal vibrations at 100 and 200 Hz
 81 are applied to a vertical hydrophobic surface with contact angle $\theta = 114 \pm 4^\circ$ (Fig.
 82 1(a)).²² A further strategy for promoting the detachment of droplets of various sizes can
 83 be adopted with cyclic variable frequency vibration. Shedding events on a
 84 superhydrophobic surface increase by 120% with this strategy.¹⁹ The positive effect of
 85 vibration on condensation has also been reported elsewhere.^{23, 24} A common feature of
 86 the above reports is they are limited to a specific frequency strongly related to the drop
 87 size. This is due to the low damping effect from reduced adhesion force between a
 88 hydrophobic surface and droplets. Careful adjustment of frequency is thus necessary,

This is the author's peer reviewed, accepted manuscript. However, the online version of record will be different from this version once it has been copyedited and typeset.

PLEASE CITE THIS ARTICLE AS DOI: 10.1063/5.0157591

Accepted to Phys. Fluids 10.1063/5.0157591

89 which also requires a complex power supply and signal processing system. Moreover,
 90 to the best of our knowledge, no literature studies the merging effect of two neighboring
 91 droplets driven by vibration.

92 Fig. 1 summarizes how our study is distinguished from the previous ones. The present
 93 study aims to experimentally and theoretically investigate the dynamics of droplet
 94 vibration on a vertical surface, with particular focus on the phase shift between two
 95 neighboring droplets at large-bandwidth frequency. Based on the theoretical model, we
 96 propose an operating strategy to enhance the coalescence of droplets of different sizes
 97 to form larger droplets which are more likely to fall. This approach is experimentally
 98 validated with a device designed to explore a large frequency spectrum. Advantages of
 99 our study include: ordinary surface without hydrophobic treatment, large bandwidth
 100 vibration instead of only the resonance frequency.

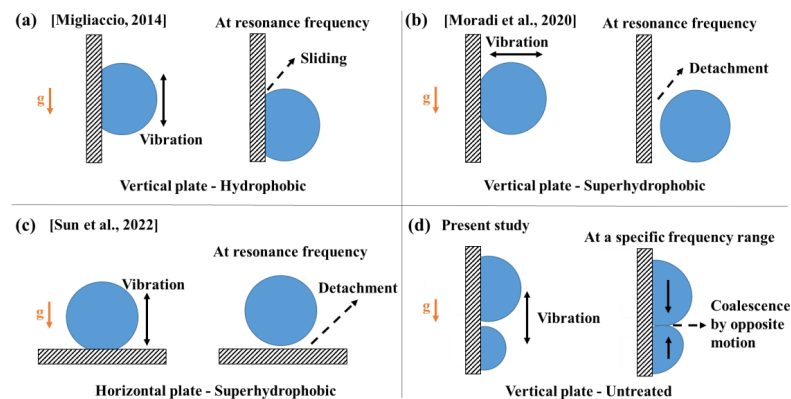


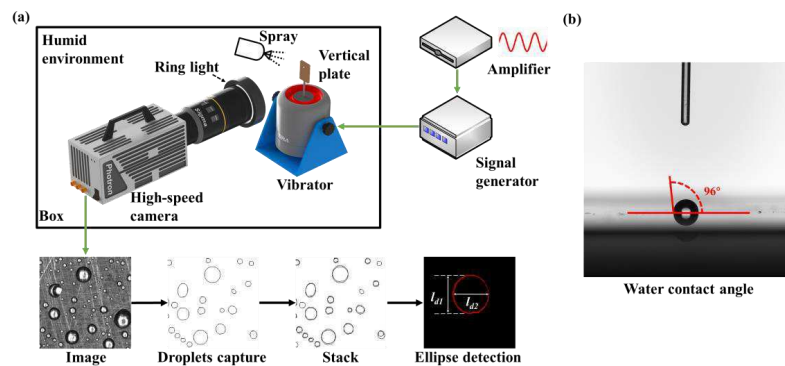
FIG. 1. Previous studies and the present study.

102
103
104 **II. Materials and methods**

105 **A. Experimental set-up**

106 The experimental set-up is shown schematically in FIG. 2(a). A sinusoidal signal is
 107 generated by a signal generator (CENTRAD GF 266) and then amplified by TIRA
 108 Analog Amplifier BAA 120. A vibrator (TIRA TV-51110) is fed by the amplified signal
 109 to vibrate a plate along its vertical axis. The copper plate studied has a contact angle of

110 about 96° (FIG. 2(b)), as measured by a contact angle system (KRÜSS DSA25B). For
 111 visualization, a high-speed camera (FASTCAM SA3) with a macro lens (Sigma
 112 MACRO 105mm F2.8 EX DG OS HSM) records the vibration of droplets on the plate
 113 at 10 000 fps (frames per second). The whole system (plate, vibrator, high-speed camera)
 114 is placed into a humidity-regulated hermetic chamber. A highly humid environment (98%
 115 RH) helps avoid the evaporation of droplets. The droplets on the plate are prepared by
 116 a sprayer and their sizes depend roughly on the number of spraying.



117

118 FIG. 2. (a) Schematic representation of the experimental setup. (b) Water-plate contact angle.

119 B. Image processing procedure

120 Image processing is performed using ImageJ²⁵ and MATLAB²⁶. Fig. 2(a) shows the
 121 main procedure from raw image to drop morphology analysis. First, sequential images
 122 from the high-speed camera are converted to binary ones after sharpening, contrast
 123 conditioning, and threshold adjustment. This allows to capture the contours of the
 124 droplets. Then two successive images, where the target droplets are in their highest and
 125 lowest positions, are stacked together. After, we get a time-averaged elliptical contour
 126 of the target droplet. Finally, the stacked image containing only the target shape is
 127 processed with MATLAB to get the dimensions of the major (l_{a1}) and minor axes (l_{a2}).
 128 Similarly, the stacking method is used to obtain the length of a fixed point (l_p) on the
 129 plate, which gives the vibration amplitude. We define a dimensionless parameter AR
 130 (Amplification Ratio) to evaluate the displacement of the center of gravity of the droplet
 131 with respect to the plate:

$$AR_e = \frac{l_{d1} - l_{d2}}{l_p} \quad (1)$$

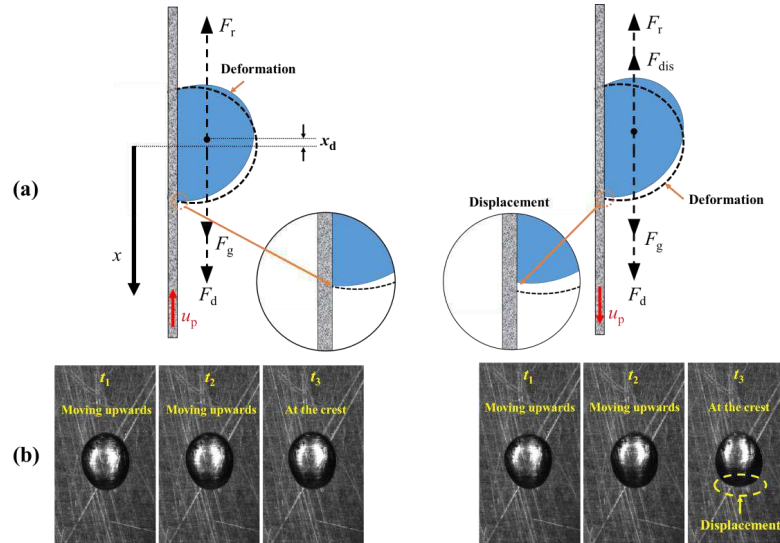
Depending on the frequency, there is a phase shift $\varphi_e \in [0, \pi]$ between the plate and a droplet. It is calculated from the difference between the two frames where the plate and the target droplet respectively start to move downward or upward.

$$\varphi_e = 2\pi \frac{\tau_p^i - \tau_d^i}{\tau_d^{i+1} - \tau_d^i} \quad (2)$$

where τ represents the sequence of frame and superscript i represents the i^{th} cycle. For example, the frames where the droplet and plate reach the crest are chosen as standard frames. Then the sequence of the standard frames for the i^{th} and $(i+1)^{\text{th}}$ cycle are used to calculate φ_e in Eq. (2).

141

142 III. Physical model of a droplet subjected to forced vibration



143

144 FIG. 3. (a) Schematic diagram of the force on a droplet without/with displacement. (b)

145 Corresponding visualization images, left: deformation only, right: deformation + displacement.

146 A generally used model to describe the drop-surface movement is the mass-spring-
147 damper system. Sarkar and Schowalter proposed a second-order ordinary differential

148 equation (ODE) model to qualitatively describe the droplet motion.^{27,28} We adapt this
 149 mass-spring-damper model to our situation to clarify the underlying mechanism of
 150 vibration-induced droplets motion (in particular, the phase shift between two droplets
 151 and their displacement). The vibrating droplet is illustrated in Fig. 3(a). We take the
 152 centroid of the droplet, without considering gravity, as the coordinate origin. Hence, in
 153 the steady state, droplets of different diameters have different displacements due to the
 154 influence of gravity. With limited plate displacement and at non-resonance frequency,
 155 the motion is the result of a balance between the driving force, F_d , the gravitational
 156 force, F_g , the restoring force, F_r , and the shear force when displacement occurs, F_{dis} .
 157 Accordingly, Newton's 2nd law of drop movement writes:

$$158 \quad m_d \frac{\partial x_d^2}{\partial t^2} = F_d + F_g + F_r + F_{dis} \quad (3)$$

159 The driving force between the wall and the droplet due to viscosity is a function of the
 160 velocity gradient and is expressed as:

$$161 \quad F_d = \mu S_U \frac{\partial u}{\partial y} = \frac{\mu S_U}{\delta} (u_p - u_d) \quad (4)$$

162 where $\delta = \sqrt{\frac{2\nu}{\omega_p}}$ is the Stokes-layer thickness with ν the kinematic viscosity,

163 $S_U = \frac{\pi d^2}{4}$ is the contact area between the bottom of the droplet and the plate, μ is the

164 dynamic viscosity, $u_d = \frac{\partial x_d}{\partial t}$ is the velocity of the droplet and $u_p = \frac{\partial x_p}{\partial t}$ is the velocity

165 of the plate where $x_p = X_p \sin(2\pi f_p t)$ is the equation of motion for the plate, with X_p
 166 the amplitude of vibration, m.

167 The gravitational force is expressed as:

$$168 \quad F_g = m_d g = \rho V_d g \quad (5)$$

169 With a given contact angle θ , the volume of the droplet V_d can be determined as²⁹:

$$170 \quad V_d = \frac{\pi d^3}{24} \left(\frac{2 - 3 \cos \theta + \cos^3 \theta}{\sin^3 \theta} \right) \quad (6)$$

171 where d is the diameter of droplet measured according to the image from the high-speed
172 camera.

173 The restoring force is calculated from the deformation of a droplet and is expressed as³⁰:

$$174 \quad F_r = -\frac{4\gamma S_\Gamma h}{d^2} (x_d - x_p) \quad (7)$$

175 where S_Γ is the droplet surface area in contact with air at equilibrium state. It is
176 determined as below:

$$177 \quad S_\Gamma = \frac{\pi d^2 (1 - \cos \theta)}{2 \sin^2 \theta} \quad (8)$$

178 In Eq. (7), h is a non-dimensional function depending on the wetting property of the
179 surface. Celestini et al.³⁰ proposed a universal curve of h according to θ ($^\circ$), expressed
180 by Eq. (9):

$$181 \quad h = -8e^{-7\theta^3} + 8e^{-5\theta^2} - 0.026\theta + 2.6589 \quad (9)$$

182 With driving frequency closer to the resonance frequency of the droplet and amplitude
183 being high enough, droplet displacement could occur. Fig. 3(b) shows images of a
184 vibrating droplet without/with displacement. In case of displacement, two issues are to
185 be corrected in the model. First, as the amplitude increases, the hypothesis of a
186 sufficiently weak external force does not hold.³⁰ Secondly, a shear force is applied to
187 the droplet due to the relative motion at the droplet-wall interface. Sellier proposed a
188 formula for the shear force by integrating the wall shear stress over the whole footprint
189 of the droplet.³¹ However, the no-slip condition and the constant droplet profile cannot
190 apply when displacement occurs. Here we propose a phenomenological equation
191 expressed like a Gaussian distribution around the resonance frequency. The shear force
192 due to displacement F_{dis} is described as:

$$193 \quad F_{dis} = -\frac{\beta}{\varepsilon\sqrt{2\pi}} e^{-\frac{(f_p - f_r)^2}{2\varepsilon^2}} (u_d - u_p) \quad (10)$$

194 where f_r is the resonance frequency of the droplet.

195 Dimensional analysis implies the units of β and ε are kg/s^2 and $1/\text{s}$ respectively.

196 Therefore, we define β as the additional tension at resonant state, which is the product

197 of the mass of the droplet and the square of its resonance frequency:

$$198 \quad \beta = m_d f_r^2 \quad (11)$$

199 The parameter ε is the standard deviation representing the influence of the additional
200 tension at resonance. Hence we define ε as the efficient frequency. After fitting
201 experimental results, we found that ε can be expressed as below:

$$202 \quad \varepsilon = \frac{f_r}{2} \quad (12)$$

203 Substituting Eqs. (4), (5), (7) and (10) into Eq. (3) yields:

$$204 \quad m_d \frac{\partial^2 x_d}{\partial t^2} = \frac{\mu S_{\text{U}}}{\delta} \left(2\pi f_p X_p \cos(2\pi f_p t) - \frac{\partial x_d}{\partial t} \right) + m_d g$$

$$- \frac{4\gamma S_{\text{O}} h}{d^2} x_d - \frac{\beta}{\varepsilon \sqrt{2\pi}} e^{-\frac{(f_p - f_r)^2}{2\varepsilon^2}} \left(\frac{\partial x_d}{\partial t} - 2\pi f_p X_p \cos(2\pi f_p t) \right) \quad (13)$$

205 Eq. (13) can be rewritten as:

$$206 \quad m_d \frac{\partial^2 x_d}{\partial t^2} + \left(\frac{\mu S_{\text{U}}}{\delta} + \frac{\beta}{\varepsilon \sqrt{2\pi}} e^{-\frac{(f_p - f_r)^2}{2\varepsilon^2}} \right) \frac{\partial x_d}{\partial t} + \frac{4\gamma S_{\text{O}} h}{d^2} x_d =$$

$$m_d g + \left(\frac{\beta}{\varepsilon \sqrt{2\pi}} e^{-\frac{(f_p - f_r)^2}{2\varepsilon^2}} + \frac{\mu S_{\text{U}}}{\delta} \right) 2\pi f_p X_p \cos(2\pi f_p t) \quad (14)$$

207 Simplifying the equation, we get:

$$208 \quad \frac{\partial^2 x_d}{\partial t^2} + 2p \frac{\partial x_d}{\partial t} + \omega_r^2 x_d = g + \frac{X'}{m_d} \cos(\omega_p t) \quad (15)$$

209 where damping ratio p and resonance frequency ω_r are determined as:

$$210 \quad p = \frac{\mu S_{\text{U}} + \frac{\beta \delta}{\varepsilon \sqrt{2\pi}} e^{-\frac{(f_p - f_r)^2}{2\varepsilon^2}}}{2\delta m_d} \quad (16)$$

$$211 \quad \omega_r = \sqrt{\frac{4\gamma S_{\text{O}} h}{m_d d^2}} \quad (17)$$

212 $f_r = \frac{\omega_r}{2\pi}$ is the resonance frequency in Hz.

213 A new time-independent parameter, X' , is used to simplify the above expression, as:

$$214 \quad X' = \left(\frac{\beta}{\varepsilon\sqrt{2\pi}} e^{-\frac{(f_p - f_r)^2}{2\varepsilon^2}} + \frac{\mu S_U}{\delta} \right) 2\pi f_p X_p \quad (18)$$

215 By solving Eq. (15) with initial conditions $u_d(0) = 0$ and $F_r(0) = m_d g$, the analytical
216 solution can be derived as:

$$217 \quad x(t) = x_H(t) + x_p(t) \quad (19)$$

218 In the above solution, $x_H(t) = e^{-pt} (C_1 \cos(\omega_r t) + C_2 \sin(\omega_r t))$ is the homogenous
219 solution with $\omega_r = \sqrt{\omega_r^2 - p^2}$. It approaches zero as steady state achieves and this term
220 could be neglected.

$$221 \quad x_p(t) = \frac{X'}{m_d \sqrt{(2\omega_p p)^2 + m_d (\omega_r^2 - \omega_p^2)^2}} \sin(\omega_p t + \phi) + \frac{g}{\omega_r^2} \text{ is the particular solution}$$

222 representing the steady-state vibration, where $X_d = \frac{X'}{m_d \sqrt{(2\omega_p p)^2 + m_d (\omega_r^2 - \omega_p^2)^2}}$ is

223 the amplitude of the droplet's center of gravity.

224 Theoretical phase shift ϕ is determined by Eq. (20):

$$225 \quad \tan \phi = \frac{-2\omega_p p}{\omega_r^2 - \omega_p^2} \quad (20)$$

226 Theoretical amplification ratio (the ratio of two amplitudes) is calculated by:

$$227 \quad AR_t = \frac{X_d}{X_p} = \frac{l_{d1} - l_{d2}}{l_p} = \frac{2\sqrt{\pi} f_p \left(\beta e^{-\frac{(f_p - f_r)^2}{2\varepsilon^2}} + \mu S_U \right)}{\delta \varepsilon m_d \sqrt{8(\omega_p p)^2 + 2m_d (\omega_r^2 - \omega_p^2)^2}} \quad (21)$$

228 Finally, another critical parameter useful for droplets merging is the distance between
229 the two borders (bottom of the upper drop and top of the lower one). The border
230 positions are roughly calculated by $X_d - d/2$ with a circular shape hypothesis.

231

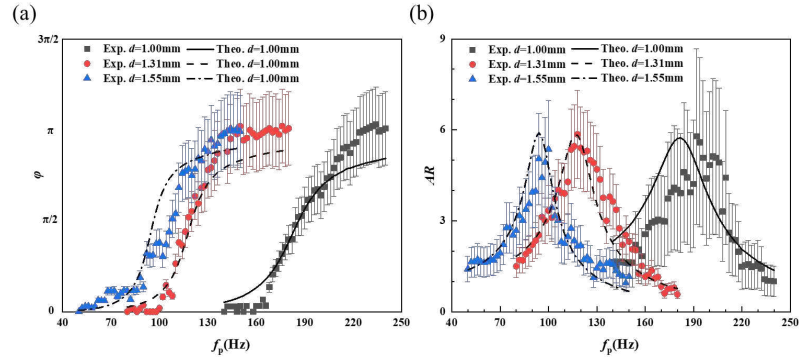
232 IV. Results and discussion

233 A. Experimental validation using the dynamic of single droplets

This is the author's peer reviewed, accepted manuscript. However, the online version of record will be different from this version once it has been copyedited and typeset.

PLEASE CITE THIS ARTICLE AS DOI: 10.1063/5.0157591

Accepted to Phys. Fluids 10.1063/5.0157591



234
 235 FIG. 4. Comparisons between theoretical (Theo.) and experimental (Exp.) results. (a) Phase shift.
 236 (b) Amplification ratio. Good agreement can be found for large droplets. For the smallest droplet
 237 at $d=1.00$ mm, the experimental AR curve shifts to the right. This is due to the influence of
 238 evaporation during the experiment.

239 We begin by investigating the dynamics of individual droplets of three different sizes
 240 (1.00, 1.31 and 1.55 mm). Different exciting frequencies from 50 to 250 Hz are applied.
 241 The natural frequency of the three droplets is respectively 183, 122, 95 Hz, inversely
 242 related to their size. For low frequencies, the motion of droplets is in phase with the
 243 plate due to the relatively higher surface tension ($\varphi = 0$). Then, a phase shift φ starts to
 244 appear from a certain frequency (defined as starting frequency f_s). φ continues to
 245 increase rapidly until the input frequency reaches a sufficiently high value (defined as
 246 inversion frequency f_i). Beyond f_i , the droplet is completely in opposite oscillation
 247 compared with the plate ($\varphi = \pi$). Fig. 4a shows similar phase shift trends for the three
 248 droplet sizes. For each droplet, the starting and inversion frequencies, f_s and f_i , are close
 249 before and after their corresponding resonance frequency. Comparing experimental and
 250 theoretical results, the maximum theoretical phase shift φ_i is slightly smaller than found
 251 experimentally. This is due to the deformation of droplet at high frequencies, which is
 252 not considered in the theoretical model. Globally, the way its trend and slope change
 253 with the input frequency in good agreement with the experiment, validates the
 254 theoretical approach.

255 Fig. 4(b) shows the amplification ratio of droplets compared with the plate oscillation
 256 amplitude. Both theoretical and experimental data show peak amplifications at around

This is the author's peer reviewed, accepted manuscript. However, the online version of record will be different from this version once it has been copyedited and typeset.

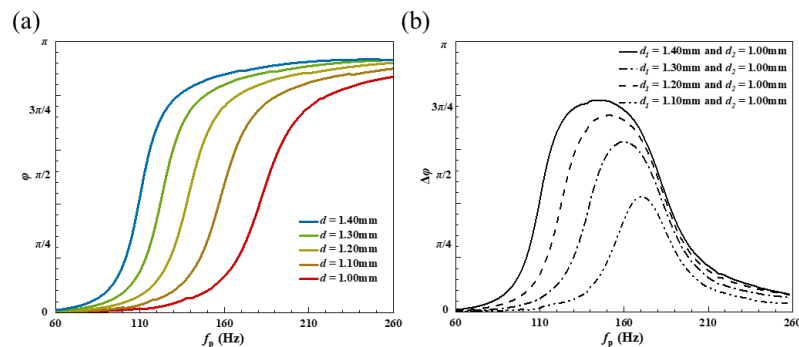
PLEASE CITE THIS ARTICLE AS DOI: 10.1063/5.0157591

Accepted to Phys. Fluids 10.1063/5.0157591

257 resonance frequency (183, 122, 95 Hz). Under our conditions, the highest value of AR
 258 is about 6, implying much stronger drop motion than the plate. The amplification ratio
 259 remains higher than 5 at a bandwidth of ~ 10 Hz around the resonance frequency. The
 260 high AR at the large-bandwidth frequency is a valuable condition to achieve drop
 261 shedding or coalescence. We discuss about it later with two droplets dynamics.
 262 In sum, experimental results fit well with theoretical ones in terms of amplification ratio
 263 and phase shift between single droplets and plate. Considering the consistency between
 264 the theoretical and experimental data, the theoretical model can be used to predict the
 265 motion of droplets in broader conditions. The following results are based on the
 266 validated theoretical model to study the behavior of neighboring droplets.

267

268 B. A strategy to promote coalescence of adjacent droplets



269

270 FIG. 5. (a) Phase shift between droplet and plate. (b) Phase shift between two adjacent droplets.

271 Fig. 5 are obtained by applying the theoretical model to five droplet sizes from 1.00 to
 272 1.40 mm. As shown in Fig. 5(a), larger droplets are more sensitive to lower frequencies
 273 due to their low resonance frequency. The starting frequency f_s and inversion frequency
 274 f_i are lower than smaller droplets. An exciting consequence is, at some specific
 275 frequency a smaller droplet can be almost in phase with the plate while a larger one is
 276 in the opposite phase. This provides condition (necessary but not sufficient) for adjacent
 277 droplets to merge. In addition, the slope of the curve rises with the increase of diameter
 278 because damping ratio p decreases for larger drop sizes.

279 Fig. 5(b) gives the theoretical phase shift between pairs of two droplets, using the 1.00
 280 mm one as a reference. The phase shift between two droplets, $\Delta\phi$, starts to be significant
 281 for larger droplets who have lower resonance frequencies. Then, $\Delta\phi$ reaches its peak
 282 value before decreasing at higher frequencies. The frequency corresponding to the peak
 283 phase shift is the optimal frequency f_{opt} to promote drop merging. For smaller droplets
 284 that are closer to the reference size, the phase shift frequency range is narrower.
 285 Moreover, the peak phase shift value decreases: it is $(3/4)\pi$ for the largest droplets pair
 286 (1.40 mm and 1 mm, near opposite motion) while only $(1/3)\pi$ for the pair 1.10 mm and
 287 1 mm. We define the continuous frequency plateau where at least 90% $\Delta\phi_{max}$ is satisfied
 288 as bandwidth. For example, between two droplets (1.10mm and 1.40mm), $f_{opt} = 133$ Hz.
 289 The $\Delta\phi$ around f_{opt} is a relatively large plateau. The whole range of [121, 146] Hz allows
 290 at least 90% maximum phase shift $\Delta\phi_{max}$. The larger of this bandwidth corresponds to
 291 ± 12.5 Hz or $\pm 9.4\%$ f_{opt} . Compared to the resonance-induced shedding, our technique
 292 offers a larger bandwidth frequency at which two neighboring droplets could coalesce.
 293 For example, Sun et al. investigates droplet detachment on a superhydrophobic surface
 294 at resonant vibration.²⁰ At the lowest amplitude, frequency range should be kept within
 295 $\pm 1\%$ of its resonance frequency ($< \pm 1$ Hz). Out of this range, the vibration surface
 296 should be amplified by +10% of the lowest amplitude. The operational bandwidth of
 297 our study is thus much larger.

298 To generalize the theory in search of the best operational condition for different drop
 299 sizes, we determine the theoretical optimal frequency f_{opt} . At this frequency, the phase
 300 shift reaches its peak value $\Delta\phi_{max}$, (c.f. Fig. 5(b)). Ideally, $\Delta\phi_{max}$ between two droplets
 301 would be π :

$$\left| \arctan \frac{-2\omega_{opt}P}{\omega_1^2 - \omega_{opt}^2} - \arctan \frac{-2\omega_{opt}P}{\omega_2^2 - \omega_{opt}^2} \right| = \pi \quad (22)$$

303 The optimal frequency $f_{opt} = \omega_{opt} / 2\pi$ can be obtained by:

$$\omega_{opt} = \sqrt{\frac{d_1\omega_1^2 + d_2\omega_2^2}{d_1 + d_2}} \quad (23)$$

305 The theoretical optimal frequencies of 22 drop size combinations are given in (Fig.

This is the author's peer reviewed, accepted manuscript. However, the online version of record will be different from this version once it has been copyedited and typeset.

PLEASE CITE THIS ARTICLE AS DOI: 10.1063/5.0157591

Accepted to *Phys. Fluids* 10.1063/5.0157591

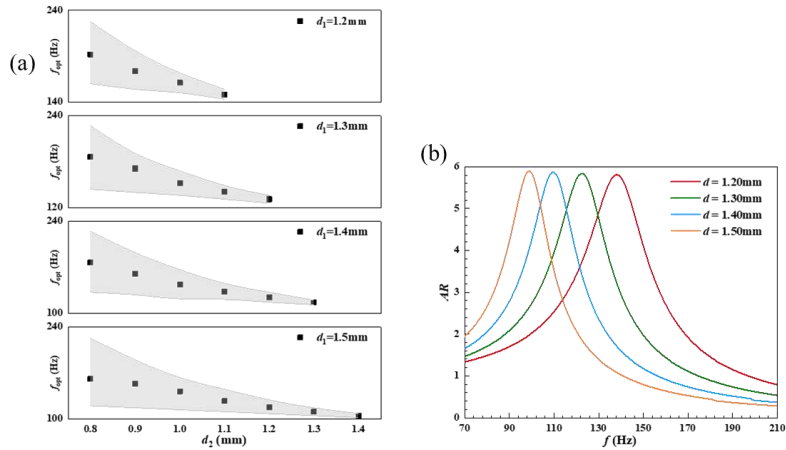
306 6(a)). The corresponding droplet sizes are $d_1 \in [1.2, 1.5]$ mm and $d_2 \in [0.8, 1.4]$ mm. One
 307 take-away message is that the optimal frequency lies between the two resonance
 308 frequencies for each droplet. Furthermore, phase shift between two droplets ($\Delta\phi$) at
 309 corresponding optimal frequency decreases as the sizes of the two droplets get similar,
 310 as listed in Tab.1. It is thus difficult to achieve an absolute opposite movement for
 311 droplets with similar sizes. It is worth noting when $d_1 = d_2$, there is no way to force them
 312 into contact by the proposed vibration technique, since they are strictly in phase
 313 whatever the frequency is.

314 In addition to $\Delta\phi$, we also need a high enough AR to promote droplets merging. Shown
 315 in Fig. 6(b) is the spectral distribution of AR for four typical drop sizes. Peak AR values
 316 correspond to the resonance frequency of one specific drop size, and are generally
 317 around 6 with our surface wetting conditions. According to the size combination, the
 318 optimal working frequency will not be at one specific resonance frequency but in
 319 between the two resonance ones. Consequently, the AR is always lower. Fortunately,
 320 the operating frequency can be adjusted within the 90% optimal frequency range
 321 without strong disturbance to the relative phase shift $\Delta\phi$. For instance, Fig. 6(a)
 322 indicates an optimal frequency between a 1.2 mm drop and a 1.5 mm one should be at
 323 118 Hz and the corresponding 90% optimal frequency range is from 108 Hz to 129 Hz.
 324 At this frequency, Fig. 6(b) gives AR s of around 3.2 and 2.3 for the two droplets
 325 respectively. If we fix the operating frequency at 108 Hz, the two AR s will be 2.4 and
 326 3.9, which holds greater potential for droplet merging.

327 Eventually, we can define the scope of application of the strategy in terms of size limit
 328 and frequency limit. The study by P. B. Weisensee et al. points out that water droplets
 329 grow mainly *via* coalescence instead of direct condensation once their diameter is larger
 330 than the effective transition one at $\sim 20 \mu\text{m}$.³⁴ With the current surface condition,
 331 theoretically it corresponds to a frequency limit of 65 kHz. The upper limit drop size
 332 can be obtained by balancing the gravitational and surface tension forces.³⁵ The average
 333 drop departure size for our surface is estimated to be ~ 1.60 mm. The corresponding
 334 frequency (lower frequency limit) is ~ 90 Hz.

This is the author's peer reviewed, accepted manuscript. However, the online version of record will be different from this version once it has been copyedited and typeset.
 PLEASE CITE THIS ARTICLE AS DOI: 10.1063/5.0157591

Accepted to Phys. Fluids 10.1063/5.0157591



335
 336 FIG. 6. (a) The optimal frequency in favor of droplet coalescence according to drop size
 337 combination. Shaded area shows the bandwidth around the optimal frequency satisfying 90%
 338 $\Delta\phi_{\max}$. (b) The frequency dependence of amplification ratio (AR) for different droplets.

339
 340 TAB. 1. Maximum phase shift between two droplets ($\Delta\phi_{\max}$) at corresponding optimal frequency.

d_1 (mm) \ d_2 (mm)	1.20	1.30	1.40	1.50
0.80	0.82π	0.85π	0.87π	0.89π
0.90	0.75π	0.80π	0.84π	0.86π
1.00	0.63π	0.73π	0.78π	0.82π
1.10	0.40π	0.60π	0.71π	0.77π
1.20		0.38π	0.58π	0.69π
1.30	0.38π		0.34π	0.56π
1.40	0.58π	0.34π		0.34π

341
 342 C. Application of the new operating strategy
 343 We use a syringe to create droplets with controllable diameters and relative position.
 344 Specifically, a smaller droplet with a diameter of 1.12 mm and a larger one with 1.39

This is the author's peer reviewed, accepted manuscript. However, the online version of record will be different from this version once it has been copyedited and typeset.

PLEASE CITE THIS ARTICLE AS DOI: 10.1063/5.0157591

Accepted to *Phys. Fluids* 10.1063/5.0157591

345 mm diameter are attached to a plate. They are aligned along the vibrating direction. The
 346 relative position of them in the x direction is 1.50 mm (center-to-center). Sinusoidal
 347 vibrations of different frequencies and amplitudes are applied to the plate and the
 348 corresponding motions of the two droplets are visualized. Slow-motion videos showing
 349 the behaviors of the two droplets at different frequencies can be found in Fig. 7
 350 (Multimedia available online).

351 The resonance frequencies f_i for the two droplets are 154 Hz and 112 Hz respectively.
 352 Our theoretical model gives an optimal frequency f_{opt} at 132 Hz and a 90% satisfactory
 353 range from 121 Hz to 143 Hz. During the experiment, we adopt three excitation
 354 frequencies at 80 Hz, 140 Hz and 260 Hz. Theoretically, the 140 Hz one is within the
 355 optimal range, while 80 Hz and 260 Hz would be either too low or too high. For $f_p=140$
 356 Hz and 260 Hz, the amplitude of plate X_p is set to 0.042 mm. For $f_p = 80$ Hz, the
 357 amplitude of the plate X_p is set to 0.085 mm. Based on the amplitude and frequency of
 358 the plate, the motion profiles of the two droplets are given in Fig. 7 (Multimedia
 359 available online). We distinguish the upper and lower limits of each droplet as well as
 360 their centers of gravity. The motion of the plate is also given. For merging purpose,
 361 special attention should be paid to the lowest limit of the upper droplet (larger one in
 362 our case) and the highest point of the bottom droplet (smaller one). The experimental
 363 keyframes are inset in the corresponding figures. At $f_p = 80$ Hz, the movements of the
 364 two droplets are almost synchronous with the movement of the plate. Therefore, the
 365 blank region between the two droplets indicate that they are in phase and cannot merge.
 366 Even if increasing the amplitude X_p , it has little effect on the blank region. At $f_p = 260$
 367 Hz, the responses of the two droplets to the vibration of plate are weak. The blank region
 368 still exists due to gentle fluctuation of two droplets and small phase shift $\Delta\varphi$.

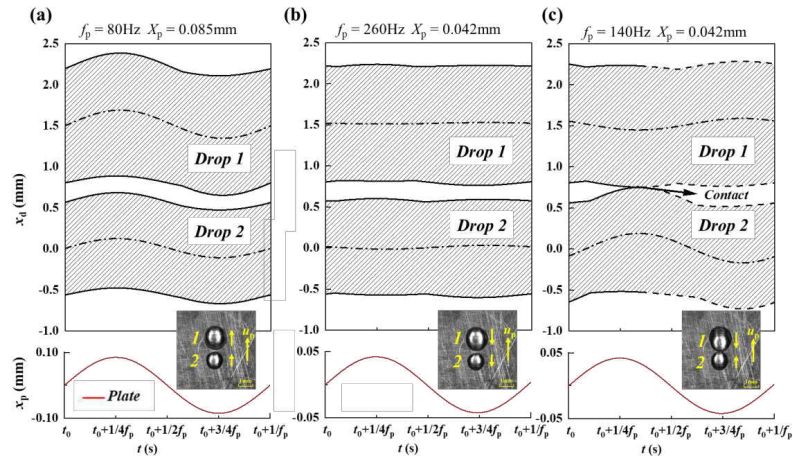
369 When $f_p = 140$ Hz, the two droplets are in totally reversed phase. The highest point of
 370 the smaller droplet and the lowest point of the larger droplet may come into contact
 371 when the plate is near the peak. The reason is that the larger droplet nearly asynchronous
 372 to the plate moves downwards while the smaller one nearly synchronous to the plate
 373 moves upwards. This produces a contrary motion which brings them together. Once the
 374 two droplets encounter each other, they merge rapidly and in an irreversible way.³²

This is the author's peer reviewed, accepted manuscript. However, the online version of record will be different from this version once it has been copyedited and typeset.

PLEASE CITE THIS ARTICLE AS DOI: 10.1063/5.0157591

Accepted to Phys. Fluids 10.1063/5.0157591

375 The process of contact is also observed in the experiment, as shown in the keyframe in
 376 Fig. 7(c) (Multimedia available online). It should be noted that the dashed line after
 377 contact represents the virtual motion because the two droplets coalesce into a new one.



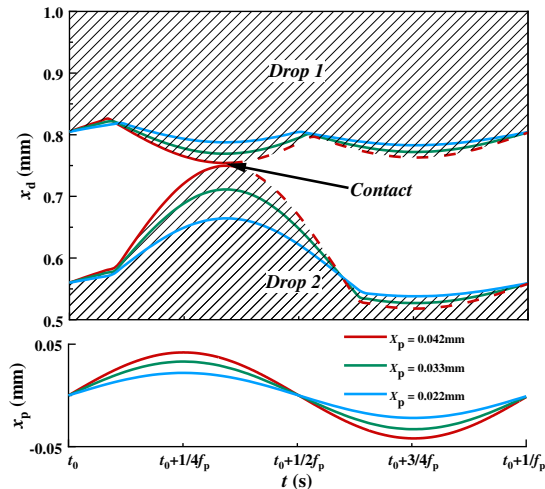
378
 379 FIG. 7. Theoretical motion curves of two droplets and experimental keyframes at different
 380 frequencies. Shaded region represents the droplet projection on the plate and dash-dotted line
 381 represents the motion curve of centers of gravity. Red lines represent the motion curve of the plate.
 382 (Multimedia available online)

383 In addition to choosing the right frequency band, high enough amplitude is also a
 384 condition to achieve droplet merging. Fig. 8 (Multimedia available online) shows the
 385 motion of the two droplets (x_d) driven by the plate (x_p) at three different amplitudes.
 386 The frequency is fixed and within the optimal frequency band. As illustrated, the motion
 387 of the larger droplet (Drop 1) is nearly opposite to the plate motion while the smaller
 388 one (Drop 2) is nearly synchronous to the plate. This property does not change as long
 389 as the frequency is fixed. At low vibration amplitude $X_p = 0.022$ mm, the responses are
 390 so mild that the two droplets remain separated. As X_p increases to 0.033 mm, the
 391 minimum distance between the two droplets reduces significantly but the two droplets
 392 still do not contact. When X_p increases to 0.042mm, their reactions further intensify so
 393 that they merge into one droplet spontaneously at the moment of approaching.

This is the author's peer reviewed, accepted manuscript. However, the online version of record will be different from this version once it has been copyedited and typeset.

PLEASE CITE THIS ARTICLE AS DOI: 10.1063/5.0157591

Accepted to Phys. Fluids 10.1063/5.0157591



394

395

396

397

398

399

400 V. Conclusion

401

402

403

404

405

406

407

408

409

410

411

412

FIG. 8. Theoretical motion curve of the two droplets at different excitation amplitudes from the plate. For drop motion x_d , only the close border lines are shown, i.e., lower limit of Drop 1 and upper limit of Drop 2. The dashed lines are virtual as merging already occurs. (Multimedia available online)

The dynamics of droplet coalescence driven by vibration on a vertical surface are experimentally and theoretically investigated. A phenomenological equation is introduced into a mass-spring-damper theoretical model to solve two problems: strong external force and additional shear force due to unpredicted slip of droplet footprint area. Results show phase shift φ occurs from size-dependent starting frequencies f_s to inversion frequencies f_i . This leads to specific optimal frequencies at which two droplets of different sizes move in opposite directions. Coupled with a high enough amplitude, these droplets may furtherly coalesce. The working frequency bandwidth is at the order of ± 10 Hz or higher, offering more chances to promote coalescence of adjacent droplets. Our findings could be helpful for the coalescence and removal of droplets. Given the droplets' size on the vertical surface, the optimal frequency can be obtained and then the vibration at the large-bandwidth frequency can be applied on the surface. The

This is the author's peer reviewed, accepted manuscript. However, the online version of record will be different from this version once it has been copyedited and typeset.

PLEASE CITE THIS ARTICLE AS DOI: 10.1063/5.0157591

Accepted to *Phys. Fluids* 10.1063/5.0157591

413 droplets coalesce and form a larger droplet which could detach from the surface. During
 414 the sliding, the droplet entrains other drops, acting as wipers. Therefore, larger
 415 uncovered surface is made available for an intensified condensation effect. Furthermore,
 416 no special hydrophobic requirement is necessary for the surface. With certain
 417 frequencies applied on the surface, the droplets of different sizes can coalesce and
 418 detach much easier. Potential applications are promising in condensation enhancement,
 419 window cleaning, photovoltaic panel cleaning, etc.

420 Although the whole study is based on a vertical surface driven by sinusoidal vibration,
 421 it can be extended to other situations. First, by simply replacing F_g by $F_g = magsin\alpha$, the
 422 developed model remains valid for inclined surfaces with an inclination angle α . Second,
 423 other forcing functions, like triangle, square, or sawtooth, can also induce droplet
 424 coalescence as they can be treated as a series of sinusoidal functions by Fourier
 425 expansion.

426
 427
 428

429 **Acknowledge**

430 The authors would like to acknowledge technical support from Frédéric Filaine. Special
 431 thanks to Dr. Eric Herbert for providing the vibration actuator, to Dr. John Lomas and
 432 Dr. Philippe Brunet for their suggestions on the manuscript. Xiangshu Lei received
 433 financial support from the CSC (China Scholarship Council). This work is also
 434 supported by the National Natural Science Foundation of China (No. 52006164).

435

436 **AUTHOR DECLARATIONS**

437 **Conflict of Interest**

438 The authors have no conflicts to disclose.

439

440 **DATA AVAILABILITY**

441 The data that support the findings of this study are available from the corresponding
 442 author upon reasonable request.

This is the author's peer reviewed, accepted manuscript. However, the online version of record will be different from this version once it has been copyedited and typeset.

PLEASE CITE THIS ARTICLE AS DOI: 10.1063/5.0157591

Accepted to *Phys. Fluids* 10.1063/5.0157591

443

444 **Reference**

445 ¹X. Li, Y. Li, R. Cai, C. Yan, X. Qiao, et al., "Insufficient condensable organic
446 vapors lead to slow growth of new particles in an urban environment," *Environ.*
447 *Sci. Technol.* 56, 9936-9946 (2022).

448 ²B. E. Fil, G. Kini, and S. Garimella, "A review of dropwise condensation: Theory,
449 modeling, experiments, and applications," *Int. J. Heat Mass Transfer* 160, 120172
450 (2020).

451 ³T. G. G. Uthpala, S. B. Navaratne, and A. Thibbotuwawa, "Review on low-
452 temperature heat pump drying applications in food industry: Cooling with
453 dehumidification drying method." *J Food Process Eng* 43, e13502 (2020).

454 ⁴Parker A. and Lawrence C., "Water capture by a desert beetle," *Nature* 414, 33-34
455 (2001).

456 ⁵B. Yang, G. Shen, H. Chen, Y. Feng, and L. Wang. "Experimental study of
457 condensation heat-transfer and water-recovery process in a micro-porous ceramic
458 membrane tube bundle," *Appl. Therm. Eng.* 155, 354-364(2019).

459 ⁶F. Macedonio, M. Frappa, A. Brunetti, G. Barbieri, and E. Drioli. "Recovery of
460 water and contaminants from cooling tower plume," *Environ. Eng. Res.* 25, 222-
461 229 (2020).

462 ⁷A. Sadeghpour, Z. Zeng, H. Ji, N. D. Ebrahimi, A. L. Bertozzi, and Y. S. Ju. "Water
463 vapor capturing using an array of traveling liquid beads for desalination and water
464 treatment," *Sci. Adv.* 5, eaav7662 (2019).

465 ⁸J. W. Rose, "Dropwise condensation theory and experiment: a review," *Proc. Inst.*
466 *Mech. Eng. A* 216, 115-128 (2002).

467 ⁹ P.-B. Bintein, H. Lhuissier, A. Mongruel, L. Royon, and D. Beysens, "Grooves
468 Accelerate Dew Shedding," *Phys Rev Lett.* 122, 098005 (2019).

469 ¹⁰C. Dorrer and J. R uhe, "Wetting of silicon nanoglass: from superhydrophilic to
470 superhydrophobic surfaces," *Adv. Mater.* 20, 159-163 (2008).

471 ¹¹J. B. Boreyko and C.-H. Chen, "Self-propelled dropwise condensate on
472 superhydrophobic surfaces," *Phys. Rev. Lett.* 103, 184501 (2009).

This is the author's peer reviewed, accepted manuscript. However, the online version of record will be different from this version once it has been copyedited and typeset.

PLEASE CITE THIS ARTICLE AS DOI: 10.1063/5.0157591

Accepted to *Phys. Fluids* 10.1063/5.0157591

- 473 ¹²X. Liu, J. Trosseille, A. Mongruel, F. Marty, P. Basset, J. Laurent, L. Royon, T.
474 Cui, D. Beysens, and T. Bourouina, "Tailoring silicon for dew water harvesting
475 panels," *iScience* 24, 102814 (2021).
- 476 ¹³R. Wen, S. Xu, X. Ma, Y.-C. Lee, and R. Yang, "Threedimensional
477 superhydrophobic nanowire networks for enhancing condensation heat transfer,"
478 *Joule* 2, 269-279 (2018).
- 479 ¹⁴J. Y. Ho, K. F. Rabbi, S. Khodakarami, J. Ma, K. S. Boyina, and N. Miljkovic,
480 "Opportunities in nano-engineered surface designs for enhanced condensation heat
481 and mass transfer," *J. Heat Transfer* 144, 050801 (2022).
- 482 ¹⁵R. Enright, N. Miljkovic, A. Al-Obeidi, C. V. Thompson, and E. N. Wang,
483 "Condensation on superhydrophobic surfaces: the role of local energy barriers and
484 structure length scale," *Langmuir* 28, 14424-14432 (2012).
- 485 ¹⁶M. Costalonga and P. Brunet. "Directional motion of vibrated sessile drops: a
486 quantitative study," *Phys. Rev. Fluid* 5, 023601 (2020).
- 487 ¹⁷H. B. Eral, D. J. C. M. 't Mannetje, and J. M. Oh, "Contact angle hysteresis: a
488 review of fundamentals and applications," *Colloid Polym Sci* 291, 247-260 (2013).
- 489 ¹⁸H. Butt, J. Liu, K. Koynov, B. Straub, C. Hinduja, I. Roismann, R. Berger, X. Li,
490 D. Vollmer, W. Steffen, and Michael Kappl, "Contact angle hysteresis," *Curr. Opin.*
491 *Colloid Interface Sci.* 59, 101574 (2022).
- 492 ¹⁹M. Moradi, S. F. Chini, and M. H. Rahimian, "Vibration-enhanced condensation
493 heat transfer on superhydrophobic surfaces: An experimental study," *AIP Adv.* 10,
494 095123 (2020).
- 495 ²⁰K. Sun, L. Shu, F. Jia, Z. Li, and T. Wang, "Vibration-induced detachment of
496 droplets on superhydrophobic surfaces," *Phys. Fluids* 34, 053319 (2022).
- 497 ²¹I. Oh, H. Cha, J. Chen, S. Chavan, H. Kong, N. Miljkovic, and Y. Hu, "Enhanced
498 condensation on liquid-infused nanoporous surfaces by vibration-assisted droplet
499 sweeping," *ACS Nano* 14, 13367-13379 (2020).
- 500 ²²C. P. Migliaccio, "Resonance-induced condensate shedding for high-efficiency
501 heat transfer," *Int. J. Heat Mass Transfer* 79, 720-726 (2014).
- 502 ²³R. A. Huber and M. M. Derby, "Droplet coalescence and departure on a vibrating

This is the author's peer reviewed, accepted manuscript. However, the online version of record will be different from this version once it has been copyedited and typeset.

PLEASE CITE THIS ARTICLE AS DOI: 10.1063/5.0157591

Accepted to *Phys. Fluids* 10.1063/5.0157591

- 503 film during humid air condensation,” 15th International Conference on
 504 Nanochannels, Microchannels, and Minichannels, New York, USA August 27-30,
 505 2017.
- 506 ²⁴L. Zhang, J. Shi, Bo Xu, and Z. Chen, “Experimental study on distribution
 507 characteristics of condensate droplets under ultrasonic vibration,” *Microgravity Sci.*
 508 *Technol.* 30, 737-746 (2018).
- 509 ²⁵C. A. Schneider, W. S. Rasband, and K. W. Eliceiri, “NIH Image to ImageJ: 25
 510 years of image analysis,” *Nat. Methods* 9, 671-675 (2012).
- 511 ²⁶MATLAB version: 9.9.0 (R2020b), Natick, Massachusetts: The MathWorks Inc.;
 512 2020.
- 513 ²⁷K. Sarkar and W. R. Schowalter, “Deformation of a two-dimensional viscoelastic
 514 drop at non-zero Reynolds number in time-periodic extensional flows,” *J. Non-*
 515 *Newtonian Fluid Mech.* 95, 315 (2000).
- 516 ²⁸K. Sarkar and W. R. Schowalter, “Deformation of a two-dimensional drop at non-
 517 zero Reynolds number in time-periodic extensional flows: numerical simulation,”
 518 *J. Fluid Mech.* 436, 177 (2001).
- 519 ²⁹Y. Yonemoto and T. Kunugib, “Estimating critical surface tension from droplet
 520 spreading area,” *Phys. Lett. A* 384, 126218 (2020).
- 521 ³⁰F. Celestini and R. Kofman, “Vibration of submillimeter-size supported droplets,”
 522 *Phys. Rev. E* 73, 041602 (2006).
- 523 ³¹M. Sellier, V. Nock, C. Gaubert, and C. Verdier, “Droplet actuation induced by
 524 coalescence: Experimental evidences and phenomenological modeling,” *Europ.*
 525 *Phys. J.-Special Topics* 219, 131-141 (2013).
- 526 ³²P. M. Somwanshi, K. Muralidhar, and S. Khandekar, “Coalescence of vertically
 527 aligned drops over a superhydrophobic surface,” *Phys. Fluids* 32, 052106 (2020).
- 528 ³³Y. Zhu, C. Tso, T. Ho, M. K. Leung, S. Yao, and H. Qiu, “Heat transfer
 529 enhancement on tube surfaces with biphilic nanomorphology,” *Appl. Therm. Eng.*
 530 180, 115778 (2020).
- 531 ³⁴P. B. Weisensee, Y. Wang, H. Qian, D. Schultz, W. P. King, and N. Miljkovic,
 532 “Condensate droplet size distribution on lubricant-infused surfaces,” *Int. J. Heat*

This is the author's peer reviewed, accepted manuscript. However, the online version of record will be different from this version once it has been copyedited and typeset.

PLEASE CITE THIS ARTICLE AS DOI: 10.1063/5.0157591

Accepted to Phys. Fluids 10.1063/5.0157591

- 533 Mass Transfer 109, 187-199 (2017).
534 ³⁵H. K. Seong, "Fabrication of Superhydrophobic Surfaces," J Adhes Sci Technol
535 22, 235-250 (2008).